Contents lists available at ScienceDirect

Chemical Engineering Research and Design

journal homepage: www.elsevier.com/locate/cherd

Optimal design of a wet-type desulphurization absorber by the numerical simulation method

Y.J. Xiao[a,b], C.T. Li[a,b,*], S.H. Li[a,b], G.M. Zeng[a,b], Q.B. Wen[a,b], G.Q. Guo[a,b], J.K. Song[a,b]

[a] College of Environmental Science and Engineering, Hunan University, Changsha 410082, PR China
[b] Key Laboratory of Environmental Biology and Pollution Control (Hunan University), Ministry of Education, Changsha 410082, PR China

ABSTRACT

Numerical study of gas–liquid flow in a wet-type desulphurization absorber is presented and the influences of different inlet and deflector structures on the device performance are identified for optimizing its structure. The dependability of numerical model is validated by the good agreement between the measured and predicted results. Besides, the results of droplet trajectories analyzed by the mechanical formulas are consistent with the simulation results as well. The performance of gas flow field is affected significantly by the inlet structures. The main reason for uneven distribution of liquid-phase is the first layer deflector rather than the gas flow. After removing the first layer deflector, the mass percentage distribution of liquid-phase in the near-wall region is reduced from 68–87% to 25–40%. The temperature distribution and relative humidity depend largely on the distribution of liquid-phase and the gas flow field. Optimized structures improve the pressure drop of device.

Keywords: Structural optimization; Two-phase flow; Temperature distribution; Liquid-phase distribution; Numerical simulation; Eulerian–Lagrangian model

1. Introduction

Air pollution, which is caused by SO_2 and dust derived from the fossil fuel combustion, has received more and more attention (Marocco, 2010; Brogren and Karlsson, 1997) recently. Especially in China, the national emission standards of air pollutants of thermal power plants are becoming increasingly stringent. For instance, the concentration of SO_2 emissions is changed from 400–1200 mg/m^3 (GB 13223-2003) to 100–400 mg/m^3 (GB 13223-2011), and the concentration of dust emission is also changed from 50–600 mg/m^3 (GB 13223-2003) to 30 mg/m^3 (GB 13223-2011). However, the traditional purification devices cannot meet the strict requirement of these limitations. Therefore, the updates of purification devices are extremely urgent. The PCF (Chinese LOGO) device is a well proven absorber of wet flue gas desulphurization (WFGD) in industrial application. With high purification efficiency, low pressure drop and perfect performance of dehydration, the PCF device is widely installed in China (Gao et al., 2010). But the unreasonable local structures make the flue gas, liquid-phase and temperature distribute unevenly in the reaction zone, which is not conducive to the mass transfer between gas and liquid in the PCF device (Tao, 2001; Dou et al., 2009). In order to further improve the purification efficiency of the PCF device, this paper presents a study of the structural optimization using CFD method to regulate the gas flow field and liquid-phase distribution.

In view of shortening development cycles and reducing development cost, it is very important to assess the performances of different setups and to confirm the influences of different design parameters in the early stages (Nova et al., 2006). In those respects, the use of numerical simulation is a key factor. In the past two decades, significant progress has been made in the mathematical model of the wet flue

* Corresponding author at: College of Environmental Science and Engineering, Hunan University, Changsha 410082, PR China. Tel.: +86 731 88649216; fax: +86 731 88649216.
E-mail addresses: ctli3@yahoo.com, ctli@hnu.edu.cn (C.T. Li).
Received 23 April 2013; Received in revised form 1 October 2013; Accepted 27 October 2013
0263-8762/$ – see front matter © 2013 The Institution of Chemical Engineers. Published by Elsevier B.V. All rights reserved.
http://dx.doi.org/10.1016/j.cherd.2013.10.026

gas desulfurization (WFGD) based on computational fluid dynamics (CFD) (Delgadillo and Rajamani, 2005; Launder and Spalding, 1972; Josserand and Zaleski, 2003; Rhodes et al., 2001). And abundant investigators employed CFD method to evaluate the performances of the hydrocyclone, fluidization bed and WFGD devices and then optimize the structural designs of them (Bernardo et al., 2006; Lu et al., 2007; Li et al., 2008; Wang and Yu, 2006). Furthermore, Nowakowski et al. (2004) elaborated the accuracy of numerical simulation and pointed out that the utilizing of numerical results in device design is advisable and promising. Comparing with the standard k–ε turbulence model which is not suitable for flow with high mean shear rate or material separation (Hoekstra et al., 1999; Wang et al., 2006), the Realizable k–ε turbulence model is more appropriate for anisotropic turbulence (Shih et al., 1995; Wang, 2004) and has been increasingly concerned in the studies of flow characteristics of the desulfurization towers (Marocco and Inzoli, 2009; Xua et al., 2013). Although the most accurate model for anisotropic turbulence is Reynolds stress model (RSM), it has the disadvantage of being more computationally expensive (Pant et al., 2002; Wang et al., 2006). Therefore, Marocco and Inzoli (2009) and Shih et al. (1995) chose the realizable k–ε turbulence model in their simulation studies and the simulation results were consistent with the experimental results very well.

Gas–liquid two-phase flow in the desulfurization tower can be simulated using the Eulerian–Eulerian and Eulerian–Lagrangian approaches (Ashraf Ali and Pushpavanam, 2011; Lu et al., 2008; Hajidavalloo et al., 2013), but the accuracy of Eulerian–Eulerian approach relies heavily on empirical constitutive equations and the effects of particle size, particle agglomeration and breakup cannot be fully taken into account (Berlemont et al., 1998; Marocco, 2010). The Eulerian–Lagrangian model, however, involves less empirical equations and is more suitable for providing detailed information of the discrete phase. Furthermore, the heat transfer between gas and liquid phase can be also taken into account easily (Marocco and Inzoli, 2009; Narasimha et al., 2005). Hence, generally, the fluid dynamics of gas–liquid phase inside the wet desulfurization tower is modeled with the Euler–Lagrange approach if the volume fraction of discrete phase is less than 10% (Buwa et al., 2006). In Eulerian–Lagrangian approach, the continuous phase is modeled in Eulerian framework (Zhang and Ahmadi, 2005), while the discrete phase is modeled with Lagrangian approach by tracking a large number of particles through the computational domain (Nowakowski et al., 2004).

Compared with experimental method, numerical simulation method is more convenient, less costly and easier to evaluate the overall performances of the device (Wang and Yu, 2006). Therefore, the gas–liquid two-phase flow in the PCF device was studied by the CFD software package (ANSYS-FLUENT) (Marocco, 2010; Jiao et al., 2006). The numerical simulations were run in a processor Xeon with 8GB RAM and every simulation took approximately 50 h. The Realizable k–ε turbulence model, the Eulerian–Lagrangian model and the SIMPLEC algorithm (Van Doormal and Raithby, 1984) were appropriately applied in these numerical simulations. The simulations focused on the influences of different inlet and deflector structures on the gas flow field, liquid-phase distribution, temperature distribution and the pressure drop. Additionally, the experiments and theoretical analyses using the Newton's second law were carried out to confirm and support the simulation results.

2. Governing equations

2.1. Carrier phase

For modeling the gas flow field in the PCF device, the incompressible Reynolds average Navier–Stokes (RANS) equations are supplemented by the realizable k–ε turbulence model. The effect of particle known as turbulence modulation is neglected due to the weak of it for low volume droplets concentration. Therefore the realizable k–ε turbulence model is used in its formulation for single-phase flows (Shih et al., 1995) and the Reynolds stress tensor is related to the average velocity gradient and turbulent viscosity of the flow following Boussinesq assumption (Marocco and Inzoli, 2009). The following equations describe the steady-state conservation equations of mass, momentum, energy and species mass, respectively:

$$\frac{\partial}{\partial x_i}(\rho_g \bar{u}_i) = 0 \tag{1}$$

$$\frac{\partial}{\partial x_j}(\rho_g \bar{u}_i \bar{u}_j) = -\frac{\partial \bar{p}}{\partial x_i} + \frac{\partial}{\partial x_j}\left[\mu \frac{\partial \bar{u}_i}{\partial x_j} - \tau_{ij}\right] + S_i \tag{2}$$

$$\frac{\partial}{\partial x_i}(\rho_g \bar{u}_i T) = \frac{\partial}{\partial x_j}\left(\frac{k + k_t}{c_P}\frac{\partial T}{\partial x_j}\right) + S_T \tag{3}$$

$$\frac{\partial}{\partial x_i}(\rho \bar{u}_i c_s) = \frac{\partial}{\partial x_j}\left(D_s \rho \frac{\partial c_s}{\partial x_j}\right) + S_s \tag{4}$$

$\tau_{ij} = \rho_g \overline{u_i' u_j'}$ is the Reynolds stress tensor which related to the average velocity gradient and turbulent viscosity of the flow. Where ρ_g is the gas density; $\bar{p}$ is the mean pressure; $\bar{u}_i$ and $\overline{u_i'}$ are the gas mean velocity and the gas mean fluctuating velocity, respectively (i, j = 1, 2, 3); T is the temperature; S_i, S_T and S_s are the source terms of momentum, energy and species, respectively; k and k_t are the molecular and turbulent thermal conductivity, respectively; c_p is the specific heat capacity; c_s is the volume concentration of component s; D_s is the diffusion coefficient of component s.

2.2. Discrete phase

Once the gas flow field is known, particle trajectory can be computed. In this study, the volume ratio of liquid-phase is less than 10%. So the liquid-phase is treated as discrete phase in the Lagrangian frame by defining the injection type, velocity, diameter and so forth (Li et al., 2008). The particle trajectory is calculated based on force balance by using the local continuous phase conditions as the particle moves along with the gas flow. These forces include the drag force, gravity and Saffman (Li et al., 2003). But the buoyancy, virtual mass and Basset term force are neglected because of the small ratio of fluid-to-particle density (Li et al., 2008; You et al., 2002). The particle–particle interaction and the effects of particle on the gas flow are also negligible due to the formulation assume that dispersed phase is sufficiently dilute. These treatments have been widely accepted for the dilute flow simulations (Buwa et al., 2006; Marocco and Inzoli, 2009; Narasimha et al., 2005). Then the momentum equation for a particle in the gas–liquid two-phase flow can be expressed as

$$\frac{du_p}{dt} = F(\bar{u} + u' - u_p) + g\frac{\rho_p - \rho_g}{\rho_p} + F_X \tag{5}$$

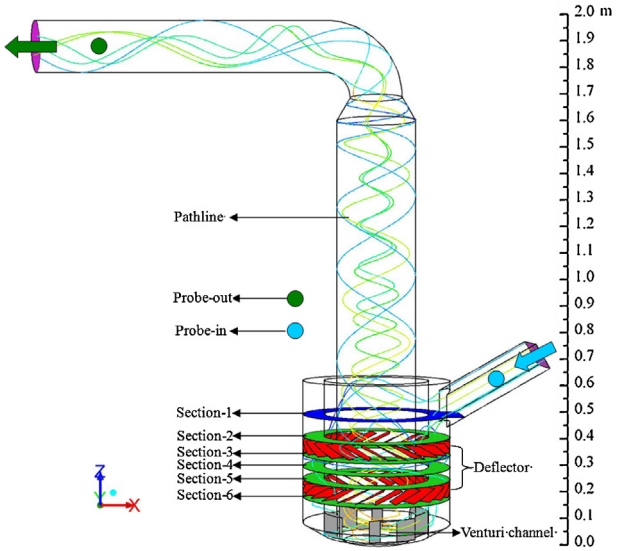

Fig. 1 – Computational domain and locations of the typical regions.

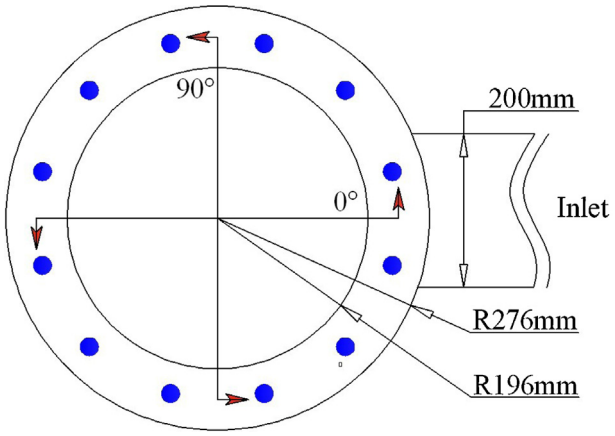

Fig. 2 – Definitions of the angles and distribution of the nozzles.

where $F(\bar{u}+u'-u_p)$ is the drag force per unit particle mass and

$$F = \frac{18\mu}{\rho_p d_p^2} C_D \frac{\rho_g d_p |\bar{u}+u'-u_p|}{24\mu} \tag{6}$$

where u' is the fluctuating velocity of gas; u_p is the particle instantaneous velocity; t is the time of particle; ρ_p is the particle density; d_p is the particle diameter; C_D is the drag coefficient and evaluated through the Morsi and Alexander (1972) correlation, $C_D = a_1 + (a_2/Re_p) + (a_3/Re_p)$; Re_p is the Reynolds number, $Re_p = \left|\bar{u}+u'-u_p\right| d_p \rho_g/\mu$; g is the gravity acceleration; F_X is the Saffman force and caused by the transverse velocity gradient of the flow.

The heating, cooling and evaporation of droplet are taken into consideration in the simulation model. Hence, the energy equation of the single droplet can be written as

$$m_p c_p \frac{dT_p}{dt} = hA_p(T_g - T_p) + \frac{dm_p'}{dt} h_{lv} \tag{7}$$

where m_p is the mass of particle; m_p' is the vaporization mass of particle; T_g and T_p are the temperature of gas and particle, respectively; A_p is the superficial area of particle; h_{lv} is the latent heat of vaporization of water; h is the heat transfer coefficient between gas and liquid phase, which is calculated by the Ranz–Marshall formula (Marocco and Inzoli, 2009)

$$Nu = \frac{hd_p}{k} = 2.0 + 0.6Re_d^{1/2}Pr^{1/3} \tag{8}$$

where Nu is the Nusselt number; Pr is the Prandtl number of continuous phase.

After the Lagrangian equations being solved using the flow properties of continuous phase, the conservation equations for continuous phase were solved again considering the influence of droplets (two-way coupling). Then, the resulting gas flow field was used for calculating the updated Lagrangian equations and so on until convergence.

3. Simulation conditions

Figs. 1 and 2 show the main configurations, dimensions, definitions of angles and some typical regions which will be mentioned in the later analysis. In the PCF device, flue gas started from the inlet flows into the preliminary treating-chamber where the gas–liquid contacted with each other and became co-flow. Gas–liquid flow though the deflectors titled in opposite directions and pass through the Venturi channel with an accelerated and rotated velocity (Gao et al., 2011b). The whole inner cylinder is used for demisting and extra demister is out of consideration. Based on the original inlet structure, other three inlet structures are devised for the PCF device. Fig. 3 shows the main configurations and dimensions of them.

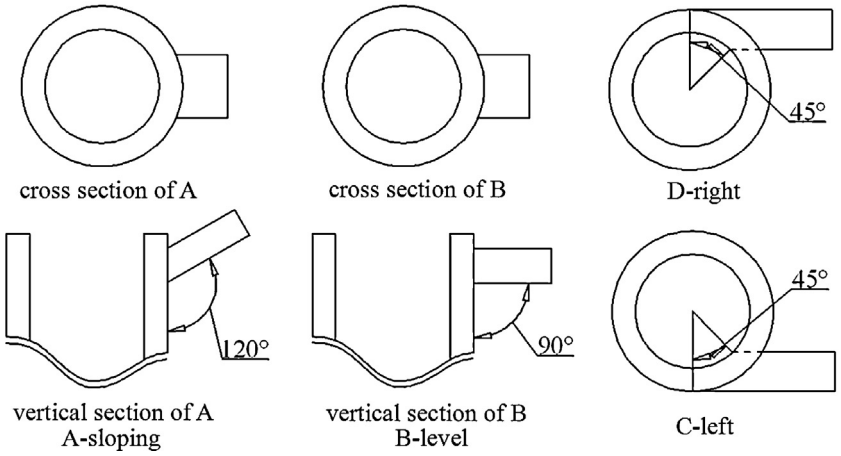

Fig. 3 – Four kinds of inlet configurations.

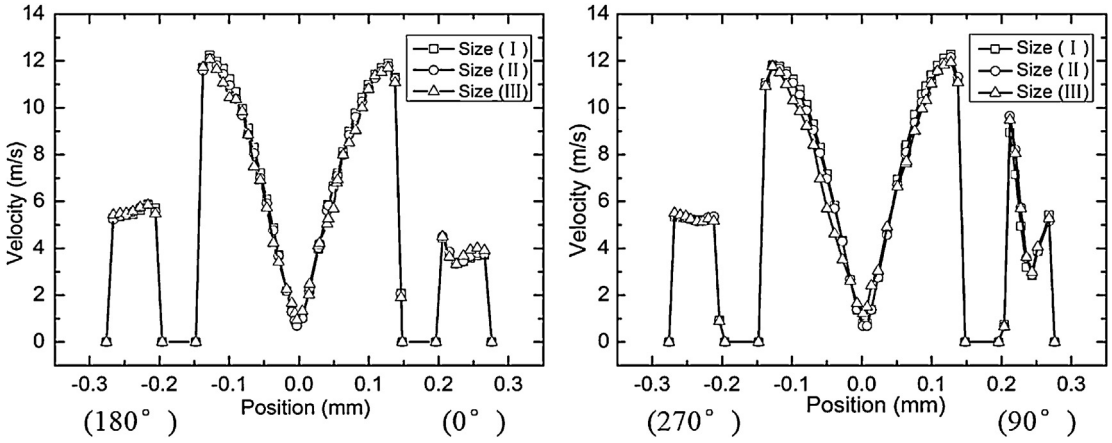

Fig. 4 – Velocity profiles of four angles at section Z = 292 mm.

Computational domain is divided by the hybrid grids (tetrahedral grid for deflectors and Venturi channel areas, hexahedral grid for other areas) and three grid sizes were tested in the preliminary studies, containing (I) – 710 000, (II) – 500 000, (III) – 360 000 cells, respectively. The simulation results of velocity profiles of four angles are revealed in Fig. 4. Although there are small differences between (III) and (II) at the positions from −0.1 m to 0 of 270°, (II) and (I) are almost the same, which suggests that the numerical result of (II) is wholly independent of the characteristics of grid (Wang et al., 2006). The difference between 0°and 90° results from the uneven distribution of flue gas in the preliminary treating chamber. The biggest sizes of tetrahedral grid and hexahedral grid of (II) are 8 mm and 10 mm, respectively.

The positions of spray nozzles are distributed at the top of preliminary treating chamber, which is shown in Fig. 2. However, the nozzles are not geometrically modeled due to the negligible impact of their dimensions on scrubber hydrodynamics when compared with other geometrical entities (Marocco, 2010). The walls are assumed to be adiabatic and the heat flux from wall to fluid is zero. Besides, the border collision type of discrete phase is reflection (Marocco, 2010; Weiss and Wieltsch, 2004). Due to a liquid film on the wall in the practice of WFGD and the small impingement angle of droplet colliding against the wall will increasing the deposition of droplet (Weiss, 2005), the reflection coefficients of normal and tangent are valued 0.1 and 0.9, respectively, which is also based on our preliminary study. The spatial discretizations for all transport equations are first order upwind at the beginning of calculation, and then the discretization schemes for pressure and momentum are changed to second order upwind when the residual curves are under 10^{-3}. Other major simulation parameters of the continuous phase and discrete phase are summarized in Table 1 (Gao et al., 2011a; Monredon et al., 1992; Marocco and Inzoli, 2009).

4. Validation tests

It is necessary to validate the model before its application to the numerical experiments. Fig. 5 shows the experimental setup of device A-1. And detailed information of the experimental setup was documented in another reference (Gao et al., 2011a). Fig. 6 presents the relationship of outlet velocities between the simulation and experiment when the flue gas velocity of entrance is 16.5 m/s. Although there is a small difference in the near-wall region between them, the results from simulation are comparable to those observed experimentally. In addition, Table 2 shows the pressure drops of experiment and simulation under different inlet velocities. The relative errors between them are very stable and range from 5% to 9%. As already found by Marocco (2010) and Weiss and Wieltsch (2004), the pressure drops with the ideal reflection model slightly over-estimate the experimental values. So, it can be concluded that the simulation results of pressure drop are in good agreement with the corresponding experimental data.

5. Results and discussion

5.1. *Gas flow field*

The distribution of gas velocity at Sect-1 (Fig. 1) is significantly affected by the varieties of inlet structure, which is shown in Fig. 7. From the comparison, the distributions of gas velocities in device C-1 and D-1 are more uniform than those in device A-1 and B-1. Therefore, it is more conducive to take full advantages of the spaces within device C-1 and D-1.

For further analyzing the characters of gas velocity distribution, the total velocities and their components of the

Table 1 – Simulation parameters of the continuous phase and discrete phase.

Continuous-phase parameters	
Inlet gas velocity	10 m/s
Inlet gas temperature	433 K
Outlet pressure	−300 Pa
Convergence residual	10^{-4}
Discrete phase parameters	
Particle treatment	Unsteady particle tracking
Particle time step size	0.002 s
Spray data	
Number of nozzles/level	12
Nozzle spray angle	45°
Nozzle type	Solid cone
Particles per nozzle	20
Spray flow/nozzle	0.2 kg/s
Liquid density (H2O)	1000 kg/m^3
Liquid temperature	300 K
Diameter distribution	Rosin–Rammler
Min diameter	0.5 mm
Max diameter	4 mm
Median diameter	2 mm
Spread parameter	3.5
Number of diameters	10

Table 2 – Comparison of the pressure drops between the experiment and simulation.

Velocity (m/s)	8.5	10	12	13.5	15	16.5	18	19.2
Experimental Δp (Pa)	182	245	360	465	575	675	795	910
Numerical Δp (Pa)	192	266	383	485	599	725	864	983

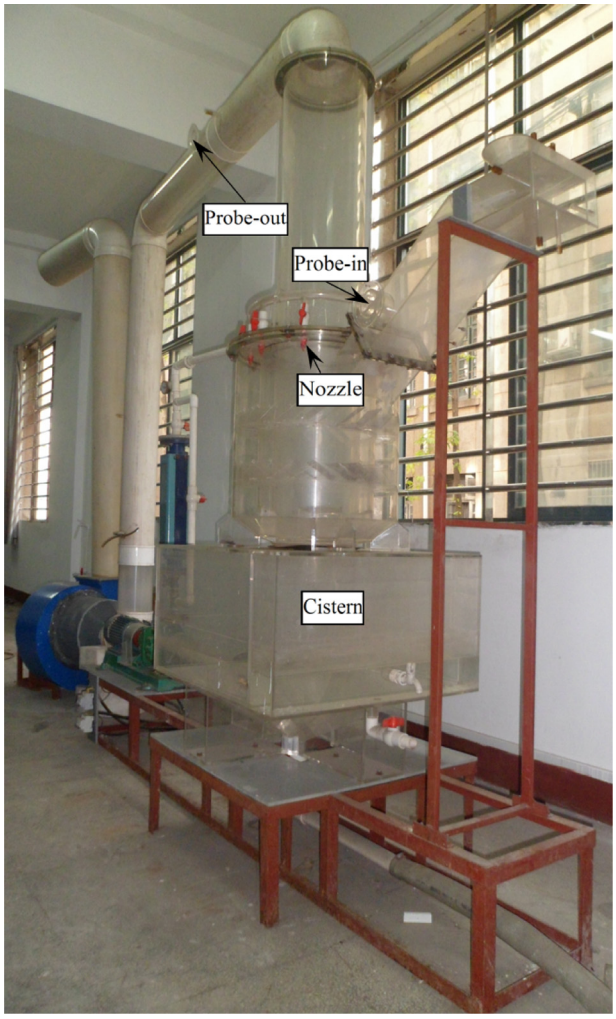

Fig. 5 – The experimental setup.

preliminary treating chamber were calculated and shown in Fig. 8. They are the average values of four straight lines along Z-axis at different angles as shown in Fig. 2. Markedly, the total velocities in device C-1 and D-1 are larger and more stable than those in device A-1 and B-1. And the tangential velocities in device C-1 and D-1 are the main components of their total velocities. As we know, fast flow rate enhances the turbulence on the surface of droplets (Hao and Prosperetti, 2004)

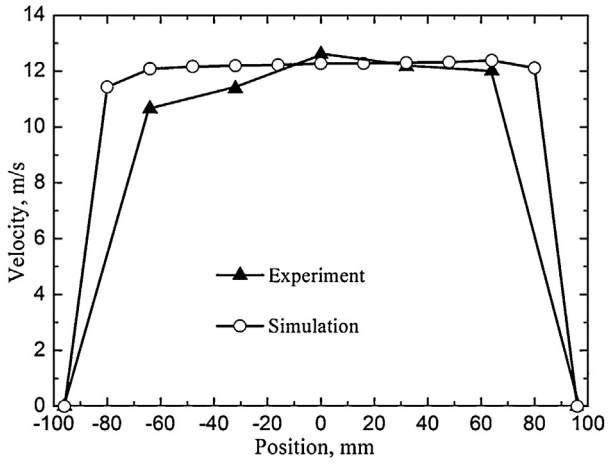

Fig. 6 – Comparison of the velocities between simulation and experiment.

and rotary movement enables the flue gas to flow through a longer path, which improves the contact of gas and liquid. The mean axial velocities of device C-1 and D-1 ($u_{axial} \approx 1.2$ m/s) are smaller than those of device A-1 and B-1 ($u_{axial} \approx 1.7$ m/s), which means the gas residence times of device C-1 and D-1 are longer than those of device A-1 and B-1. The gas-side mass-transfer coefficient is evaluated by the Sherwood number (Marocco and Inzoli, 2009; Kiel et al., 1993)

$$Sh = 2.0 + 0.6Re_d^{1/2}Sc^{1/3} \tag{9}$$

where Sc is the Schmidt number. Sh constantly increases with the increasing of $u = |\bar{u} + u' - u_p|$, which can be deduced from $Re_p = ud_p\rho_g/\mu$. So in device C-1 and D-1, the heat and mass transfer between gas and liquid is promoted due to the u of them are bigger than those of device A-1 and B-1 (Fu et al., 2013; Bokotko and Hupka, 2005). Furthermore, stokes number S_{tk} is a parameter showing the effect of inertial impaction which is one of the dust removal mechanism of the wet desulphurization and dedusting process (Tardos et al., 1979). The S_{tk} can be wrote as

$$S_{tk} = \frac{C\rho_s d_s^2 u}{18\mu d_p} \tag{10}$$

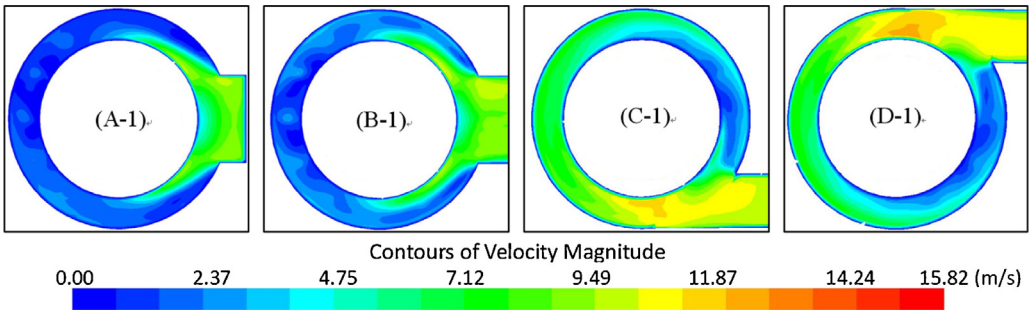

Fig. 7 – Flue gas velocity at Sect-1 in different inlet structures (A-1 – sloping inlet, B-1 – level inlet, C-1 – left inlet, and D-1 – right inlet).

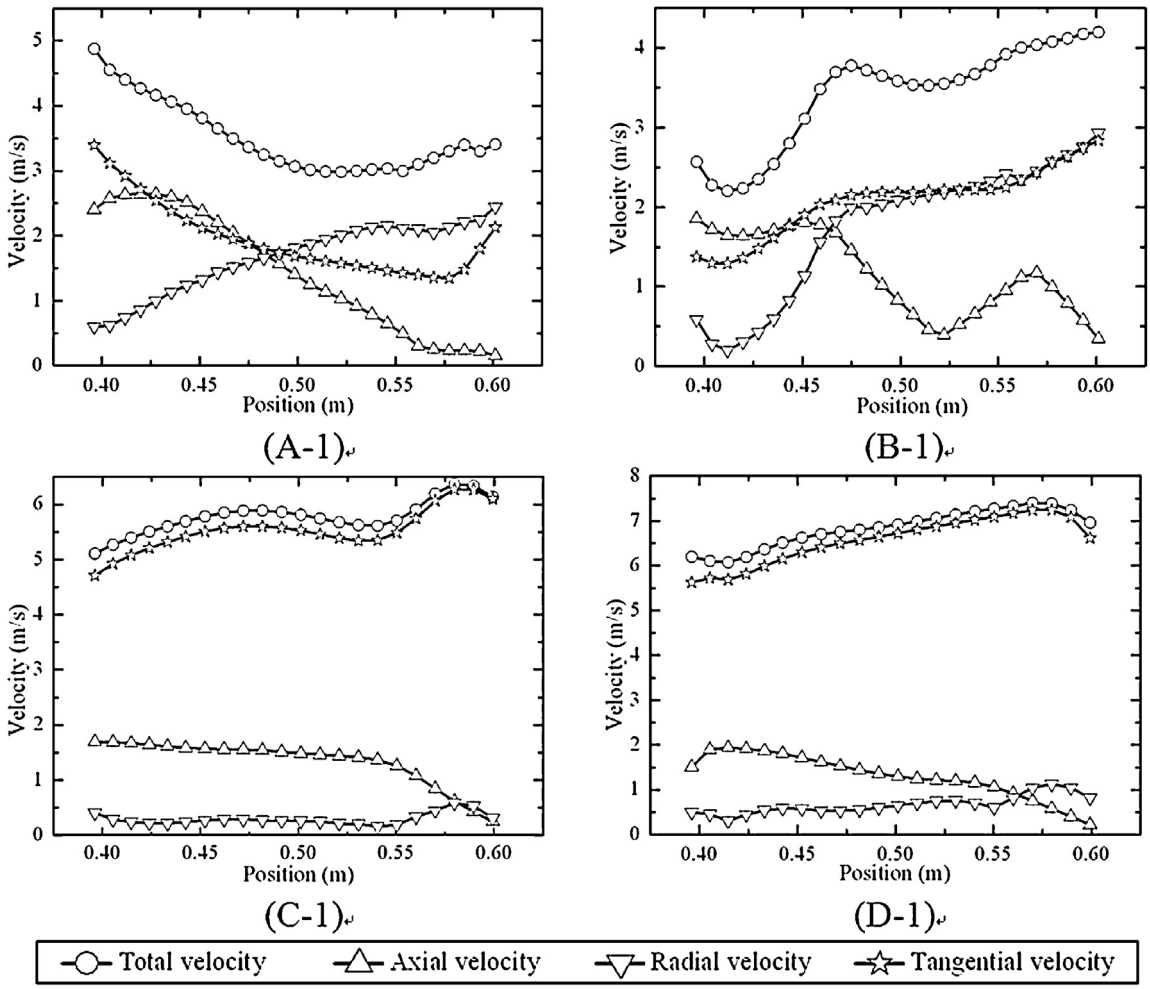

Fig. 8 – Total, axial, radial and tangential velocity profiles of the preliminary treating chambers.

where C is the coefficient; ρ_s and d_s are the density and diameter of dust, respectively. There is a positive linear relationship between the effect of inertial impaction and $u = |\bar{u} + u' - u_p|$. Therefore, the inlet structures of device C-1 and D-1 improve the performance of gas flow field.

5.2. *Liquid-phase distribution*

5.2.1. *Theoretical analysis of force*

When a droplet keeps moving in the preliminary treating chamber, the drag force F of tangential direction acting on the droplet by the gas flow can be written as

$$F = \frac{C_D \pi \rho_g d_p^2 u^2}{8} \tag{11}$$

In the above equation, u is the relative tangential velocity between gas and liquid, $u = |u_{g,tangential} - u_{p,tangential}|$; C_D is the drag coefficient which is a function of Reynolds number $Re_p = ud_p\rho_g/\mu$ (Wang et al., 2006). In device C-1 and D-1, the particle motion of tangential direction belongs to turbulent state because of $500 < Re_p = 550 < 2 \times 10^5$ ($u \approx 6$ m/s, $d_p = 2$ mm, $\rho_{g(T=353\,K)} = 1$ kg/m^3, $\mu_{T=353\,K} = 2.18 \times 10^{-5}$). So $C_D \approx 0.44$, $F = 0.055\pi\rho_g d_p^2 u^2$ and the particle acceleration $a_{D=2\,mm} \approx 5.9$ m/s^2. In device A-1 and B-1, the particle motion of tangential direction belongs to turbulent transition state because of $1 < Re_p = 183 < 500$ ($u \approx 2$ m/s, $d_p = 2$ mm, $\rho_{g(T=353\,K)} = 1$ kg/m^3, $\mu_{T=353\,K} = 2.18 \times 10^{-5}$). So $C_D = 18.5/Re_p^{0.6}$, $F = (18.5/8)\pi\rho_g^{0.4}\mu^{0.6}d_p^{1.4}u^{1.4}$ and $a_{D=2\,mm} \approx 0.78$ m/s^2. F is changed dramatically among the different devices due to the gas flow. But the changes of droplet trajectories are not obvious due to a short time (after spraying, most of the droplets with high velocity collide against the deflector within 0.03–0.05 s), i.e. the gas flows do not promote the collisions between the droplets and wall or deflector in the studied devices. But, if the size of purification apparatus increases within a wide range, the effects of gas flow acting on the droplets cannot be ignored.

5.2.2. *Simulation results*

Mass percentage distribution of the liquid-phase is shown in Fig. 9. Although there are some small localized differences of the mass percentage distribution among device A-1, B-1, C-1 and D-1, the trends of overall distributions of Sect-2 and Sect-3 in device C-1 and D-1 are similar to those in device A-1 and B-1. It can be explained by the fact that the effects of gas flow on the particle trajectory are not obvious in the studied devices, which is certified by Eq. (11). On the other hand, they occupy a large proportion of the mass percentage distribution in the near-wall regions (268 mm < R < 276 mm) of Sect-4 in all devices. It is the result of the droplets which do not collide against the first layer deflector being forced to have a large tangential velocity and moving outward to the wall very quickly due to the centrifugal force acting on them (Jiao et al., 2006). Therefore, the device cannot take full advantages of the huge specific surface areas which generated by the spray nozzles. As we all know, the distribution of liquid-phase is the main factor

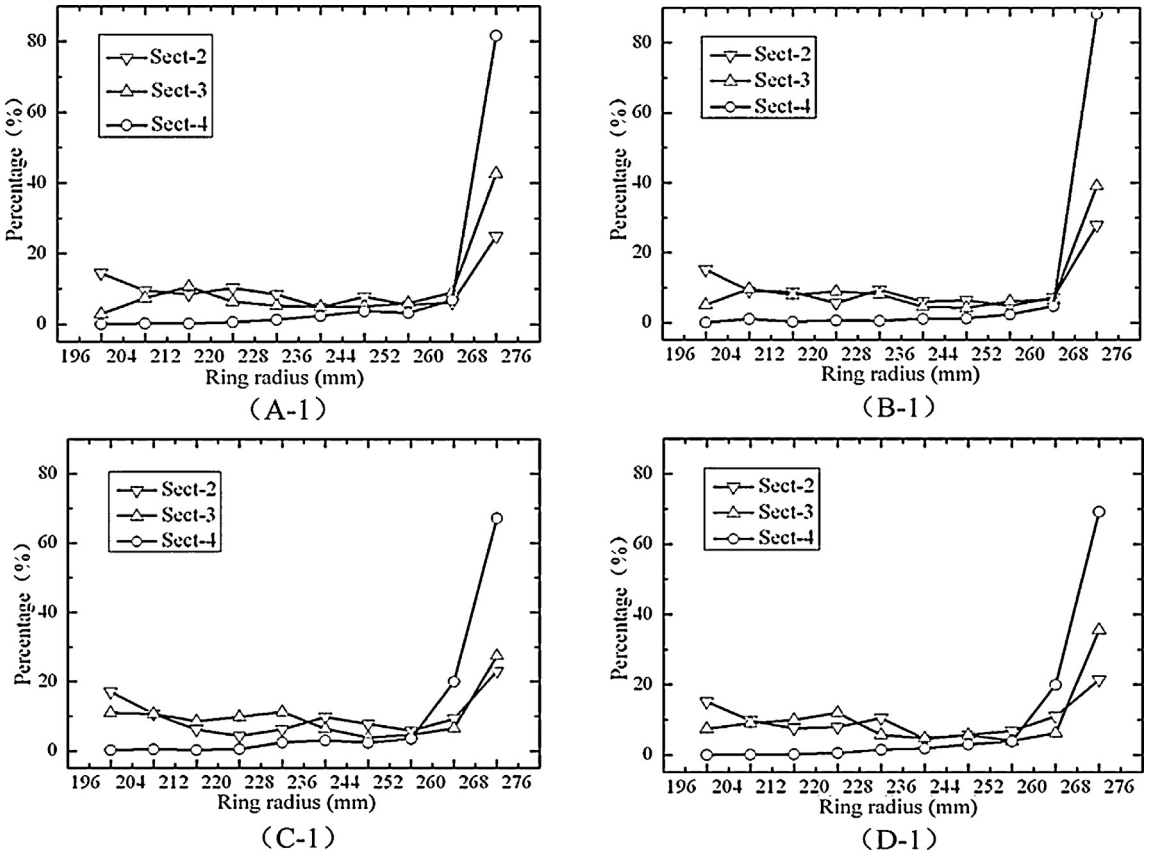

Fig. 9 – Mass percentage distribution of the liquid-phase.

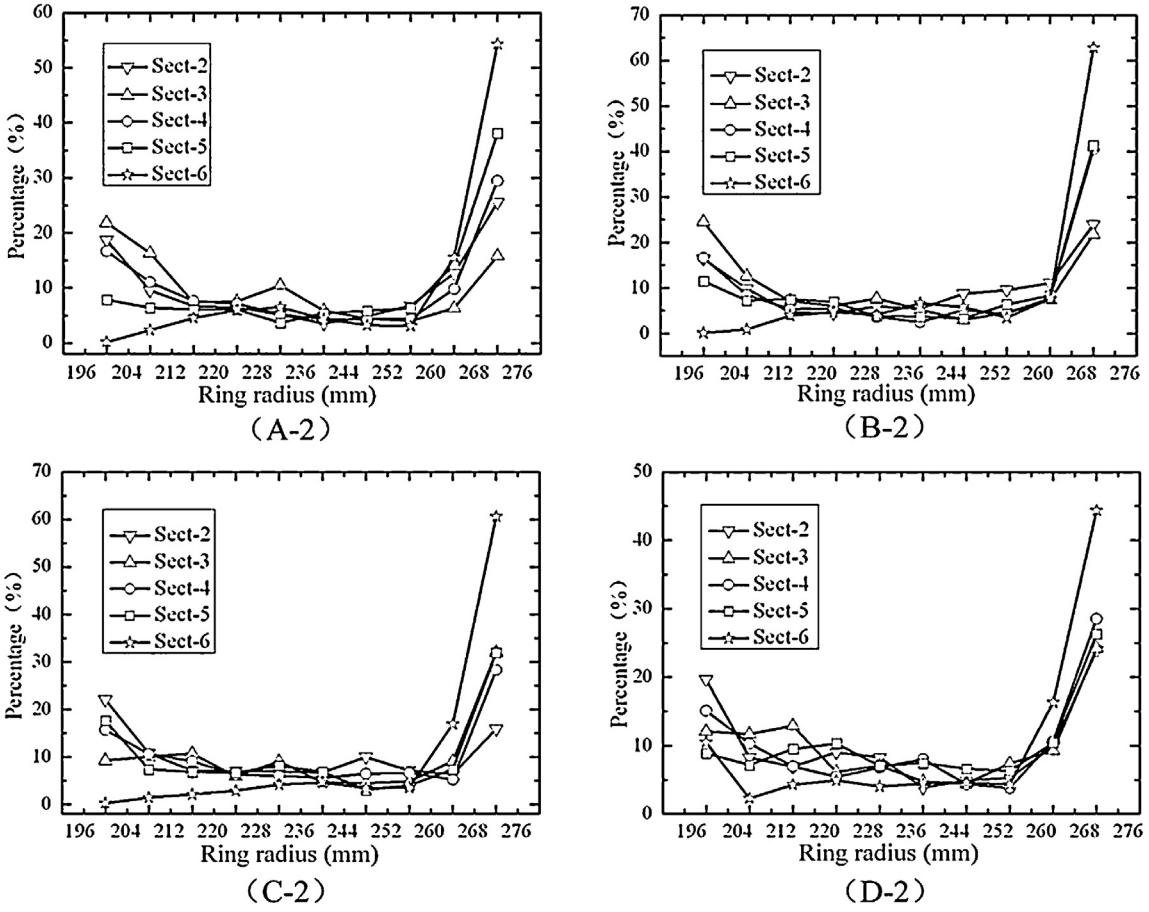

Fig. 10 – Mass percentage distribution of the liquid-phase (A-2, B-2, C-2 and D-2 – without the first layer deflector).

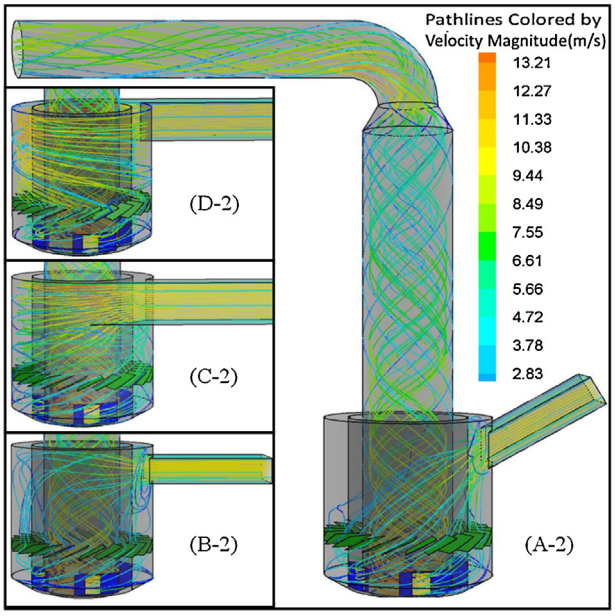

Fig. 11 – Path line of the gas flow.

of desulphurization and dedusting (Neveux and Moullec, 2011; Warych and Szymanowski, 2001). So it is possible to make further optimization for these devices by removing the first layer deflector.

5.2.3. *Performances of the optimized devices*

The mass percentage distributions of the liquid-phase in the optimized devices without the first layer deflector are illustrated in Fig. 10. In device C-2 and D-2, the distributions of Sect-4 and Sect-5 are similar to those of Sect-2 and Sect-3 after removing the first layer deflector. And the distributions of Sect-6 concentrate in the near-wall region due to the influence of second layer deflector in all devices, which means a good performance of dehydration. Once again, these conclusions certify that the main reason for uneven distribution of liquid-phase is the first layer deflector rather than the gas flow. At the same time, the uniformity of flue gas and the rate of tangential velocity in device A-2 and B-2 become less competitive than those in device A-1 and B-1. But the flue gas in device C-2 and D-2 do not change significantly and they are still good for desulphurization and dedusting, which is shown in Fig. 11. Therefore, the effects of structural optimization are

Table 3 – Pressure drops of the eight devices (u_{in} = 10 m/s).

Device	A-1	B-1	C-1	D-1	A-2	B-2	C-2	D-2
Δp (Pa)	257.6	250	335.4	253	206	202	223	282

significant for device C-2 and D-2, which results in the mass percentage distributions of Sect-2, Sect-3, Sect-4 and Sect-5 becoming more reasonable and conducive to desulphurization and dedusting.

5.3. *Distribution of gas temperature*

Fig. 12 shows the flue gas temperature of device A-1 and C-2. In device A-1, the temperature of inlet region is very high, but the distribution of near wall region is low, which results from the gas- and liquid-phase distributions. So, the distribution of temperature in device C-2 is more desirable than that in device A-1, which is consistent with the conclusions of gas flow field and liquid-phase distribution of device C-2. Besides, the heat transfer between gas- and liquid-phase is very fast (Marocco and Inzoli, 2009) and takes place at the upper part of the preliminary treating chamber. The rate of heat transfer between gas and liquid can be deduced from the equation of $Q = \zeta(T_g - T_p) + m'_p h_{l_v}$ (Tao, 2001), ζ is the coefficient of heat transfer. The temperature distinction between flue gas and droplet is huge when the gas enters the tower, which results in the temperature dropping dramatically. The relative humidity of the flue gas increasing up to saturation with the evaporation of droplet is shown in Fig. 13. The changes of relative humidity are closely related with the changes of temperature in the numerical simulation, which is also confirmed by the numerical and experimental study of Marocco and Inzoli (2009).

5.4. *Pressure drop*

The pressure drops of all devices, obtained by the numerical simulation, are displayed in Table 3. The pressure drops decrease in these devices without the first layer deflector except for device D-2, which is the result of high-speed flue gas frontally colliding against the deflector in device D-2. Although the pressure drop of device C-2 is slightly larger than those of device A-2 and B-2, the performance of device C-2 is desirable for the industrial application.

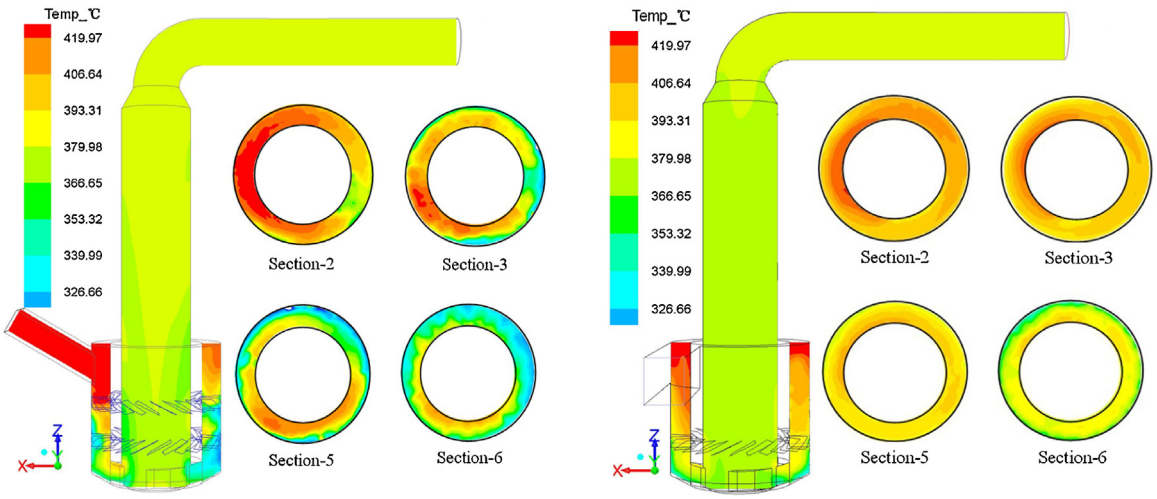

Fig. 12 – Flue gas temperature of section Y = 0 and four horizontal sections.

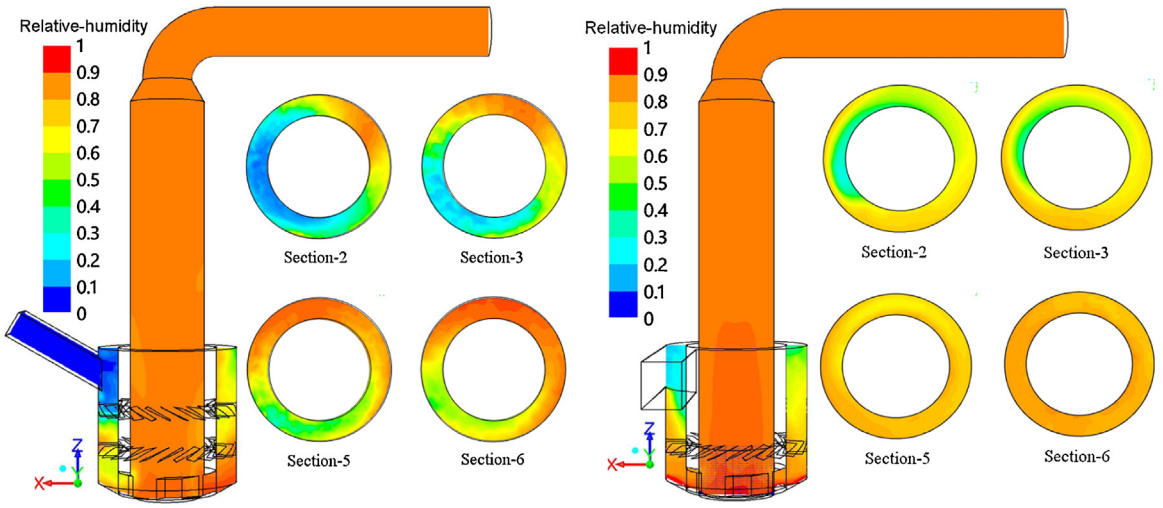

Fig. 13 – Relative humidity of section Y = 0 and four horizontal sections.

6. Conclusions

This study proposes some optimal designs for the PCF device. A fluid dynamics model for calculating the distributions of gas- and liquid-phase was developed. The calculated values of velocity and pressure drop agree well with the experimental data under different operating conditions. Factors affecting the performance of device are presented, analyzed and discussed. The following conclusions can be drawn from the results obtained in this study.

The value and uniformity of gas flow field in the preliminary treating chamber are changed significantly due to the different inlet structures. Greater tangential velocities do not make the distributions of liquid-phase become more uneven in the optimized devices, and the first layer deflector is the main reason for uneven distribution. So the distribution of liquid-phase is significantly improved after removing the first layer deflector. Combining the advantages of gas- and liquid-phase distributions, the temperature distribution and relative humidity become more uniform and conducive for the desulfurization in device C-2. The pressure drop of device C-2 is also competitive among all devices. The optimized structures and the simulation results could provide guidance for the research of equipment design and the update of installed PCF device.

Acknowledgments

This work was supported by the National High Technology Research and Development Program of China (863 Program, No. 2011AA060803), the Scientific and Technological Major Special Project of Hunan Province in China (No. 2010XK6003), the Project supported by National Natural Science Foundation of China (Nos. 51278177, 51108168), the Science and Technology Department of Project in Hunan Province (2012RS4001) and the Project supported by Hunan Provincial Natural Science Foundation (13JJ3044).

References

Ashraf Ali, B., Pushpavanam, S., 2011. Analysis of unsteady gas–liquid flows in a rectangular tank: comparison of Euler–Eulerian and Euler–Lagrangian simulations. Int. J. Multiphase Flow 37, 268–277.

Berlemont, A., Chang, Z., Gouesbet, G., 1998. Particle Lagrangian tracking with hydrodynamic interactions and collisions. Flow Turbul. Combust. 60, 1–18.

Brogren, C., Karlsson, H.T., 1997. Modeling the absorption of SO_2 in a spray scrubber using the penetration theory. Chem. Eng. Sci. 52, 3085–3099.

Bernardo, S., Mori, M., Peres, A.P., 2006. 3-D computational fluid dynamics for gas and gas-particle flows in a cyclone with different inlet section angles. Powder Technol. 162, 190–200.

Buwa, V.V., Deo, D.S., Ranade, V.V., 2006. Eulerian–Lagrangian simulations of unsteady gas–liquid flows in bubble columns. Int. J. Multiphase Flow 32, 864–885.

Bokotko, R.P., Hupka, J., 2005. Flue gas treatment for SO_2 removal with air-sparged hydrocyclone technology. Environ. Sci. Technol. 39, 1184–1189.

China department of Environmental Protection, 2011. Emission Standard of Air Pollutants for Thermal Power Plants (GB 13223-2011). China Environmental Science Press http://kjs.mep.gov.cn/hjbhbz/bzwb/dqhjbh/dqgdwrywrwpfbz/201109/W020130125407916122018.pdf

Dou, B.L., Pan, W.G., Jin, Q., Wang, W.H., Li, Y., 2009. Prediction of SO_2 removal efficiency for wet flue gas desulfurization. Energy Convers. Manage. 50, 2547–2553.

Delgadillo, J.A., Rajamani, R.K., 2005. A comparative study of three turbulence-closure models for the hydrocyclone problem. Int. J. Miner. Process. 77, 217–230.

Fu, B., Liu, B.T., Yuan, X.G., Chen, S.Y., Yu, K.S., 2013. Modeling of Rayleigh convection in gas–liquid interfacial mass transfer using lattice Boltzmann method chemical engineering research and design. Chem. Eng. Res. Des. 91, 437–447.

Gao, H.L., Li, C.T., Zeng, G.M., Zhang, W., Shi, L., Li, S.H., Zeng, Y.N., Fan, X.P., Wen, Q.B., Shu, X., 2010. Prediction and experimental validation studies of wet flue gas desulphurization with a novel type PCF device based on limestone-gypsum. Energy Fuels 24, 4944–4951.

Gao, H.L., Li, C.T., Zeng, G.M., Zhang, W., Shi, L., Li, S.H., Zeng, Y.N., Fan, X.P., Wen, Q.B., Shu, X., 2011a. Flue gas desulphurization based on limestone–gypsum with a novel wet-type PCF device. Sep. Purif. Technol. 76, 253–260.

Gao, H.L., Li, C.T., Zeng, G.M., Zhang, W., Shi, L., Fan, X.P., Zeng, Y.N., Wen, Q.B., Shu, X., 2011b. Experimental study of wet flue gas desulphurization with a novel type PCF device. Chem. Eng. Process. 50, 189–195.

Hajidavalloo, E., Sadeghi-Behbahani-Zadeh, M., Shekari, Y., 2013. Simulation of gas–solid two-phase flow in the annulus of drilling well. Chem. Eng. Res. Des. 91, 477–484.

Hao, Y., Prosperetti, A., 2004. A numerical method for three-dimensional gas–liquid flow computations. J. Comput. Phys. 196, 126–144.

Hoekstra, A.J., Derksen, J.J., Van Den Akker, H.E.A., 1999. An experimental and numerical study of turbulent swirling flow in gas cyclones. Chem. Eng. Sci. 54, 2055–2056.
Josserand, C., Zaleski, S., 2003. Droplet splashing on a thin liquid film. Phys. Fluids 15, 1650–1657.
Jiao, J.Y., Zheng, Y., Sun, G.G., Wang, J., 2006. Study of the separation efficiency and the flow field of a dynamic cyclone. Sep. Purif. Technol. 49, 157–166.
Kiel, J.H.A., Prins, W., Van Swaaijw, P.M., 1993. Mass Transfer between gas and particles in a gas–solid trickle flow reactor. Chem. Eng. Sci. 48, 117–125.
Lu, H.L., Zhao, Y.H., Ding, J.M., Dimitri, G., Li, W., 2007. Investigation of mixing segregation of mixture particles in gas-solid fluidized beds. Chem. Eng. Sci. 62, 301–317.
Li, S.H., Li, C.T., Zeng, G.M., Li, S.M., Wang, F., Wang, D.Y., Lu, P., 2008. Simulation and experimental validation studies on a new type umbrella plate scrubber. Sep. Purif. Technol. 62, 323–329.
Launder, B.E., Spalding, D.B., 1972. Lectures in Mathematical Models of Turbulence. Academic Press, London.
Lu, J., Fugal, J.P., Nordsiek, H., Saw, E., Shaw, R., Yang, W., 2008. Lagrangian particle tracking in three dimensions via single-camera in-line digital holograph. New J. Phys. 10, 2–24.
Li, X.D., Yan, J.H., Cao, Y.C., Ni, M.J., Cen, K.F., 2003. Numerical simulation of the effects of turbulence intensity and boundary layer on separation efficiency in a cyclone separator. Chem. Eng. J. 95, 235–240.
Morsi, S.A., Alexander, A.J., 1972. An investigation of particle trajectories in two-phase flow systems. J. Fluid Mech. 55, 193–208.
Monredon, T.C., Hsieh, K.T., Rajamani, R.K., 1992. Fluid flow model of the hydrocyclone: an investigation of device dimensions. Int. J. Miner. Process. 35, 65–83.
Marocco, L., 2010. Modeling of the fluid dynamics and SO_2 absorption in a gas–liquid reactor. Chem. Eng. J. 162, 217–226.
Marocco, L., Inzoli, F., 2009. Multiphase Euler–Lagrange CFD simulation applied to wet flue gas desulphurisation technology. Int. J. Multiphase Flow 35, 185–194.
Nowakowski, A.F., Cullivan, J.C., Williams, R.A., Dyakowski, T., 2004. Application of CFD to modelling of the flow in hydrocyclone. Is this a realizable option or still a research challenge? Miner. Eng. 17, 661–669.
Narasimha, M., Sripriya, R., Banerjee, P.K., 2005. CFD modelling of hydrocyclone – prediction of cut size. Int. J. Miner. Process. 75, 53–68.
Nova, I., Ciardelli, C., Tronconi, E., 2006. NH_3-SCR of NO over a V-based catalyst: low-T redox kinetics with NH_3 inhibition. AIChE J. 52, 3222–3233.
Neveux, T., Moullec, Y.L., 2011. Wet industrial flue gas desulfurization unit: model development and validation on industrial data. Ind. Eng. Chem. Res. 50, 7579–7592.
Pant, K., Crowe, C.T., Irving, P., 2002. On the design of miniature cyclone for the collection of bioaerosols. Powder Technol. 125, 260–265.
Rhodes, M.J., Wang, X.S., Nguyen, M., Stewart, P., Liffman, K., 2001. Study of mixing in gas-fluidized beds using a DEM model. Chem. Eng. Sci. 56, 2859–2866.
State Environmental Protection Administration, 2003. Emission Standard of Air Pollutants for Thermal Power Plants (GB 13223-2003). China Environmental Science Press.
Shih, T.-H., Liou, W.W., Shabbir, A., Yang, Z.G., Zhe, J., 1995. A new κ–ε eddy-viscosity model for high Reynolds number turbulent flows. Comput. Fluids 24, 227–238.
Tao, W.Q., 2001. Numerical Heat Transfer, second ed. Xi'an Jiaotong University Press, Xi'an (in Chinese).
Tardos, G.I., Yu, E., Pfeffer, R., Squires, A.M., 1979. Experiments on aerosol filtration in granular sand beds. J. Colloid Interface Sci. 71, 616–621.
Van Doormal, J.P., Raithby, G.G., 1984. Enhancement of the SIMPLE method for predicting incompressible fluid flows. Numer. Heat Transfer 7, 147–163.
Weiss, C., Wieltsch, U., 2004. Laser optical flow measurements and computational fluid dynamic calculation of spray tower hydrodynamics. Chem. Eng. Res. Des. 83, 1–17.
Weiss, C., 2005. The liquid deposition fraction of sprays impinging vertical walls and flowing films. Int. J. Multiphase Flow 31, 115–140.
Wang, F.J., 2004. Computational Fluid Dynamics: Principles and Applications. Tsinghua University Press, Beijing (in Chinese).
Warych, J., Szymanowski, M., 2001. Model of the wet limestone flue gas desulfurization process for cost optimization. Ind. Eng. Chem. Res. 40, 2597–2605.
Wang, B., Xu, D.L., Chu, K.W., Yu, A.B., 2006. Numerical study of gas–solid flow in a cyclone separator. Appl. Math. Model. 30, 1326–1342.
Wang, B., Yu, A.B., 2006. Numerical study of particle–fluid flow in hydrocyclones with different body dimensions. Miner. Eng. 19, 1022–1033.
Xua, Y.Y., Zhang, Y., Wang, J.C., Yuan, J.Q., 2013. Application of CFD in the optimal design of a SCR–DeNO_x system for a 300 MW coal-fired power plant. Comput. Chem. Eng. 49, 50–60.
You, C.F., Qi, H.Y., Xu, X.C., 2002. Progresses and applications of basset force. Chin. J. Appl. Chem. 19, 31–33 (in Chinese).
Zhang, X.Y., Ahmadi, G., 2005. Eulerian–Lagrangian simulations of liquid–gas–solid flows in three-phase slurry reactors. Chem. Eng. Sci. 60, 5089–5104.